Neutron capture on ^{94}Zr: Resonance parameters and Maxwellian-averaged cross sections

G. Tagliente,[1,2,*] P. M. Milazzo,[3] K. Fujii,[3] U. Abbondanno,[3] G. Aerts,[4] H. Álvarez,[5] F. Alvarez-Velarde,[6] S. Andriamonje,[4] J. Andrzejewski,[7] L. Audouin,[8] G. Badurek,[9] P. Baumann,[10] F. Bečvář,[11] F. Belloni,[3] E. Berthoumieux,[4] S. Bisterzo,[12] F. Calviño,[13] M. Calviani,[14] D. Cano-Ott,[6] R. Capote,[15,16] C. Carrapiço,[17] P. Cennini,[18] V. Chepel,[19] E. Chiaveri,[18] N. Colonna,[1] G. Cortes,[13] A. Couture,[20] J. Cox,[20] M. Dahlfors,[18] S. David,[10] I. Dillmann,[8] C. Domingo-Pardo,[21] W. Dridi,[4] I. Duran,[5] C. Eleftheriadis,[22] M. Embid-Segura,[6] A. Ferrari,[18] R. Ferreira-Marques,[19] W. Furman,[23] R. Gallino,[12] I. Goncalves,[19] E. Gonzalez-Romero,[6] F. Gramegna,[14] C. Guerrero,[6] F. Gunsing,[4] B. Haas,[24] R. Haight,[25] M. Heil,[8] A. Herrera-Martinez,[18] E. Jericha,[9] F. Käppeler,[8] Y. Kadi,[18] D. Karadimos,[26] D. Karamanis,[26] M. Kerveno,[10] E. Kossionides,[27] M. Krtička,[11] C. Lamboudis,[22] H. Leeb,[9] A. Lindote,[19] I. Lopes,[19] M. Lozano,[16] S. Lukic,[10] J. Marganiec,[7] S. Marrone,[1] T. Martínez,[6] C. Massimi,[28] P. Mastinu,[14] A. Mengoni,[15] C. Moreau,[3] M. Mosconi,[8] F. Neves,[19] H. Oberhummer,[9] S. O'Brien,[20] J. Pancin,[4] C. Papachristodoulou,[26] C. Papadopoulos,[29] C. Paradela,[5] N. Patronis,[26] A. Pavlik,[30] P. Pavlopoulos,[31] L. Perrot,[4] M. T. Pigni,[9] R. Plag,[8] A. Plompen,[32] A. Plukis,[4] A. Poch,[13] J. Praena,[14] C. Pretel,[13] J. Quesada,[16] T. Rauscher,[33] R. Reifarth,[25] M. Rosetti,[34] C. Rubbia,[35] G. Rudolf,[10] P. Rullhusen,[32] J. Salgado,[17] C. Santos,[17] L. Sarchiapone,[18] I. Savvidis,[22] C. Stephan,[36] J. L. Tain,[21] L. Tassan-Got,[36] L. Tavora,[17] R. Terlizzi,[1] G. Vannini,[28] P. Vaz,[17] A. Ventura,[34] D. Villamarin,[6] M. C. Vincente,[6] V. Vlachoudis,[18] R. Vlastou,[29] F. Voss,[8] S. Walter,[8] M. Wiescher,[20] and K. Wisshak[8]

[1]*Istituto Nazionale di Fisica Nucleare (INFN), Bari, Italy*
[2]*University of Gent, Belgium*
[3]*Istituto Nazionale di Fisica Nucleare (INFN), Trieste, Italy*
[4]*CEA/Saclay–IRFU, Gif-sur-Yvette, France*
[5]*Universidade de Santiago de Compostela, Spain*
[6]*Centro de Investigaciones Energeticas Medioambientales y Technologicas, Madrid, Spain*
[7]*University of Lodz, Lodz, Poland*
[8]*Forschungszentrum Karlsruhe GmbH (FZK), Institut für Kernphysik, Germany*
[9]*Atominstitut der Österreichischen Universitäten, Technische Universität Wien, Austria*
[10]*Centre National de la Recherche Scientifique/IN2P3-IReS, Strasbourg, France*
[11]*Faculty of Mathematics and Physics, Charles University in Prague, Czech Republic*
[12]*Dipartimento di Fisica Generale, Università di Torino, Italy*
[13]*Universitat Politecnica de Catalunya, Barcelona, Spain*
[14]*Istituto Nazionale di Fisica Nucleare (INFN), Laboratori Nazionali di Legnaro, Italy*
[15]*International Atomic Energy Agency (IAEA), NAPC/Nuclear Data Section, Vienna, Austria*
[16]*Universidad de Sevilla, Spain*
[17]*Instituto Tecnológico e Nuclear (ITN), Lisbon, Portugal*
[18]*CERN, Geneva, Switzerland*
[19]*LIP-Coimbra & Departamento de Fisica da Universidade de Coimbra, Portugal*
[20]*University of Notre Dame, Notre Dame, Indiana 46556, USA*
[21]*Instituto de Física Corpuscular, CSIC–Universidad de Valencia, Spain*
[22]*Aristotle University of Thessaloniki, Greece*
[23]*Joint Institute for Nuclear Research, Frank Laboratory of Neutron Physics, Dubna, Russia*
[24]*Centre National de la Recherche Scientifique/IN2P3-CENBG, Bordeaux, France*
[25]*Los Alamos National Laboratory, Los Alamos, New Mexico 87545, USA*
[26]*University of Ioannina, Greece*
[27]*NCSR, Athens, Greece*
[28]*Dipartimento di Fisica, Università di Bologna, and Sezione INFN di Bologna, Italy*
[29]*National Technical University of Athens, Greece*
[30]*Institut für Fakultät für Physik, Universität Wien, Austria*
[31]*Pôle Universitaire Léonard de Vinci, Paris La Défense, France*
[32]*CEC-JRC-IRMM, Geel, Belgium*
[33]*Department of Physics and Astronomy, University of Basel, Basel, Switzerland*
[34]*ENEA, Bologna, Italy*
[35]*Università degli Studi di Pavia, Pavia, Italy*
[36]*Centre National de la Recherche Scientifique/IN2P3-IPN, Orsay, France*

(Received 26 August 2010; revised manuscript received 22 April 2011; published 15 July 2011)

The neutron capture cross sections of the Zr isotopes play an important role in nucleosynthesis studies. The *s*-process reaction flow between the Fe seed and the heavier isotopes passes through the neutron magic nucleus ^{90}Zr and through ^{91,92,93,94}Zr, but only part of the flow extends to ^{96}Zr because of the branching point at ^{95}Zr. Apart from their effect on the *s*-process flow, the comparably small isotopic (n, γ) cross sections make Zr also

an interesting structural material for nuclear reactors. The ^{94}Zr (n, γ) cross section has been measured with high resolution at the spallation neutron source n_TOF at CERN and resonance parameters are reported up to 60 keV neutron energy.

DOI: 10.1103/PhysRevC.84.015801 PACS number(s): 25.40.Lw, 25.70.Ef, 27.60.+j, 28.41.Qb

I. INTRODUCTION

The production of heavy elements in stars is almost exclusively due to neutron capture processes named for the time scales at which they take place: the rapid (r) process is related to explosive scenarios, e.g., supernovae and neutron star mergers, with extremely hot (temperatures $T > 10^9$ K) and neutron-rich (neutron densities $n_n \gg 10^{20}$ cm^{-3}) environments, where neutron capture times are of the order of milliseconds. In contrast, the slow (s) process occurs during the He burning phases of stellar evolution at lower temperatures [$T \approx (1–3) \times 10^8$ K] and much lower neutron densities ($n_n \approx 10^6–10^{10}$ cm^{-3}) with typical capture times of about a year [1]. The terms slow and rapid refer to the average β-decay half-lives close to the valley of stability.

In massive stars neutrons are produced by the ^{22}Ne$(\alpha, n)^{25}$Mg reaction during the presupernova evolution, i.e. during convective core helium burning and convective carbon shell burning [2]. These stars contribute only to the s abundances below $A = 90$ by the so-called weak s process. The s abundances from Zr to Bi constitute the main s component and are produced in thermally pulsing low-mass asymptotic giant branch (AGB) stars, which populate the mass region $1.5 \leqslant M/M_\odot \leqslant 3$ (where $M_\odot$ denotes the mass of the Sun) [3–5]. Zr is, therefore, situated at a crucial point, where these two s components match.

The isotopes 90–94 are characterized by low neutron capture cross sections and are predominantly of s-process origin. Because of the comparably short half-life of ^{95}Zr ($t_{1/2} = 64d$) the competition between neutron capture and β^- decay prevents the main part of the reaction flow from reaching ^{96}Zr, which is, therefore, considered an r isotope with a small s-process admixture [6,7]. Any significant s production of ^{96}Zr would imply that the stellar neutron density is high enough for neutron capture on ^{95}Zr to compete with the β decay.

As a result of the efficient transport mechanisms between the He burning layers and the outer envelope, significant s-process enrichments have been spectroscopically observed in AGB stars. Among the refractory compounds that can be formed at the comparatively low surface temperatures of these red giant stars, ZrO has also been identified. Studies of molecular bands of ZrO confirmed the expected s-process pattern for the Zr isotopes, with a ^{96}Zr abundance that was missing or at most compatible with the solar value within the observational uncertainties [8]. Similar indications come from the isotopic Zr abundances in presolar silicon carbide grains [9], which are formed from s-process-enriched material in the circumstellar envelopes of AGB stars [10]. These grains also show a deficiency in ^{96}Zr compared to stellar model predictions based on theoretically calculated ^{95}Zr cross sections [11].

The deficiency of the molecular ^{96}Zr lines in the optical spectra of AGB stars as well as the low ^{96}Zr abundances in presolar grains provide evidence that the ^{95}Zr branching is weaker than expected, because either the s-process neutron density or the (n, γ) cross section of ^{95}Zr has been overestimated so far. This ambiguity in the assessment of the ^{95}Zr branching calls for a more accurate set of Zr cross sections [12–14] for an improved assessment of the ^{95}Zr branching.

Apart from the problem with the ^{95}Zr branching, ^{94}Zr is important for the decomposition of the solar abundance pattern into the relative s and r components, because it is the Zr isotope with the highest s-process contribution [15]. In order to be used as reference isotope for this separation of the s and r components, the capture cross section of ^{94}Zr is needed with an uncertainty of 3%–5%, a typical request for meaningful s-process analyses [16].

The (n, γ) cross sections of the Zr isotopes are also of interest for technological applications due to the common use of Zr as a structural material in nuclear technology, where it contributes to the neutron balance, the lifetime, and the overall performance of power reactors.

The ^{94}Zr(n, γ) cross section has been measured up to 60 keV neutron energy using the unique features of the n_TOF facility at CERN, which combines excellent resolution, high instantaneous neutron flux, and low background [17]. The measurement is described in Sec. II, followed by the resonance analysis and the results in Sec. III. The Maxwellian-averaged capture cross sections (MACSs) and the implications for the s-process abundance are discussed in Secs. IV and V.

II. MEASUREMENT

A. Experimental setup

At the CERN n_TOF facility neutrons are produced by spallation reactions induced by a pulsed proton beam with 6 ns pulse width and a nominal repetition rate of 0.4 Hz in a massive lead block of $80 \times 80 \times 60$ cm^3. Due to the high beam momentum of 20 GeV/c, which provides 300 neutrons per proton, and the high intensity of 7×10^{12} protons per pulse, the n_TOF facility represents one of the most luminous pulsed neutron sources worldwide [17]. The initially fast spallation neutrons are moderated in the 5.8-cm-thick layer of cooling water around the lead target, resulting in a wide neutron spectrum ranging from thermal up to 250 MeV with a nearly constant isolethargic flux [$\phi(E) \propto 1/E$] between 1 eV and 1 MeV.

The lead spallation target is connected with the experimental area at a flight path of 185 m by an evacuated beamline. Neutrons and ultrarelativistic particles outside the beamline are suppressed by heavy concrete walls and a massive iron shielding 3.5 m in thickness. In addition, charged particles are removed from the neutron beam by a 1.5 T sweeping

*giuseppe.tagliente@ba.infn.it

TABLE I. Sample characteristics.

Sample	Chemical form	Isotopic composition (%)				
		^{90}Zr	^{91}Zr	^{92}Zr	^{94}Zr	^{96}Zr
^{94}Zr	ZrO_2	4.05	1.18	1.93	91.8	1.04

magnet [18]. The neutron beam is collimated in two steps, at 140 m and near 175 m, shortly before the last shielding wall in front of the experimental area. The 18 mm aperture of the second collimator gives rise to a nearly symmetric Gaussian-shaped beam profile at the sample position. The spatial distribution of the beam has been measured as a function of neutron energy [19], and the neutron flux was accurately determined relative to the ^{235}U(n, f) cross section by means of a calibrated fission chamber from PTB Braunschweig [17]. Additional flux measurements were carried out with parallel-plate avalanche counters [20] and by the analysis of standard resonances [21].

The measurement was performed between 1 eV and 60 keV with a resolution in neutron energy of better than 0.2%. The flux of 10^5 neutrons/cm^2/pulse was constantly recorded by a low-mass neutron monitor consisting of a Mylar foil 1.5 μm in thickness with a layer of 200 μg/cm^2 of ^{6}Li. The monitor was located 1.5 m upstream of the capture samples. The ejectiles from the ^{6}Li$(n, \alpha)^3$H reaction were detected by a set of four Si detectors surrounding the sample outside the neutron beam [22]. Calibration runs with a gold reference sample were conducted at regular intervals for additional checks of the neutron beam.

Capture events were detected via the prompt γ-ray cascades with a pair of C_6D_6 liquid scintillator cells, which were optimized for accurate measurements of resonance-dominated (n, γ) cross sections [23]. The thin carbon fiber cells are directly glued onto an EMI-9823QKB photomultiplier tube, thus reducing the detector mass as much as possible. This design and the very low capture cross sections of deuterium, carbon, oxygen, and silicon, which are the main constituents of the scintillator and the detectors, resulted in a correspondingly small neutron sensitivity of less than 10^{-5}. We recall that the neutron sensitivity of the capture setup is particularly important in this measurement, considering the large scattering/capture ratio that characterizes ^{94}Zr.

The detectors were mounted perpendicular to the neutron beam, which was 4 cm in diameter at this point, and at a distance of about 3 cm from the axis. Background due to in-beam γ rays produced by neutron capture in the spallation target and predominantly in the water moderator [18] was reduced by placing the detectors 9.2 cm upstream of the sample position.

The light output of the detectors was calibrated at 662, 1173, and 1332 keV with ^{137}Cs and ^{60}Co reference sources. An additional calibration point at 6.13 MeV was obtained by means of a composite ^{238}Pu/^{13}C source. The calibrations were repeated at regular intervals to verify the stability of the detectors and of the data acquisition system.

To extract the neutron energy the time of flight to energy relation of Ref. [21] was used.

The data acquisition system was based on fast digitizers operating at 500×10^6 MSamples/s with a memory option to store the detector output for each neutron burst over a time-of-flight (TOF) interval of 16 ms, corresponding to a lower limit in neutron energy of 0.7 eV. The data from the digitizers were reduced by a zero-suppression routine and the remaining signals were stored for off-line analysis of the deposited γ-ray energy in the scintillator and the respective TOF [24].

The ^{94}Zr sample was prepared from ZrO_2 powder with an enrichment of 91.8%. The powder was pressed to a pellet 22 mm in diameter, 1.3 mm in thickness, and 2.015 g in mass. The pellet was canned in an aluminum capsule with 0.1-mm-thick walls and a mass of about 300 mg. The sample contained impurities of Hf, Sn, Na, Mg, and Al, which contributed 0.01% to the total weight. Various of the observed resonances in the TOF spectra could be assigned to the impurities, in particular to Hf and Sn. This background contribution was carefully taken into account in data analysis.

In addition to ^{94}Zr, a Au and a Pb sample were also mounted on the carbon fiber sample changer used in the experiment. Au was used for monitoring the neutron flux; the Pb sample served for the determination of the background. The sample characteristics are summarized in Table I.

B. Capture yields

The γ-ray spectrum and the corresponding cascade multiplicity depend on the isotope under study and may even change from resonance to resonance for a given isotope. To detect capture events independently of the cascade multiplicity, the intrinsic efficiency of C_6D_6 detectors has to be corrected by the pulse height weighting technique (PHWT) [25–27]. The PHWT consists of an off-line modification of the response function of the detector, which is constructed to modify the detector efficiency such that it increases linearly with γ-ray energy. In this case, the efficiency for capture cascades becomes proportional to the total released γ energy.

The experimental capture yields are obtained by means of weighting functions (WFs), which are parametrized as polynomial functions of the γ-ray energy. Each recorded detector signal is multiplied with the proper WF to obtain the required linearity with γ-ray energy. This transformation of the raw data is valid if the efficiency of the detector is low enough to detect only one γ ray per capture event. This requirement is met by the C_6D_6 detectors because of their low intrinsic efficiency and their restricted solid angle, resulting in an overall efficiency for the detection of capture events of $\approx$20%. The detailed geometry and nuclear composition of the experimental setup have been implemented in Monte Carlo simulations and the weighting functions were determined, following the prescriptions outlined in Ref. [27].

To obtain the absolute yield the measured yield has been normalized by applying the saturated resonance technique, using a 0.1-mm-thick Au sample [28].

Once the fraction of incident neutrons undergoing (n,γ) reactions in the sample is defined, the capture yield is directly linked to the capture and total cross sections.

C. Backgrounds

The identification and characterization of all possible backgrounds is important because the capture cross section of ^{94}Zr is relatively small. The different background components are due to (i) capture events in the detectors or in surrounding materials caused by neutrons scattered from the sample, (ii) capture events in the aluminum can of the Zr sample, (iii) in-beam γ rays produced in the spallation target, and (iv) the ambient background in the experimental area.

(i) This contribution to the background was evaluated by means of the carbon sample, which can be considered as a pure scatterer. Thanks to the very low neutron sensitivity of the setup [17,23], the neutron scattering effect on the Zr resonances is practically negligible.

(ii) Measurements with an empty Al can showed that this component is also very small, except for a few well-known Al resonances, which were identified and subtracted from the Zr spectra.

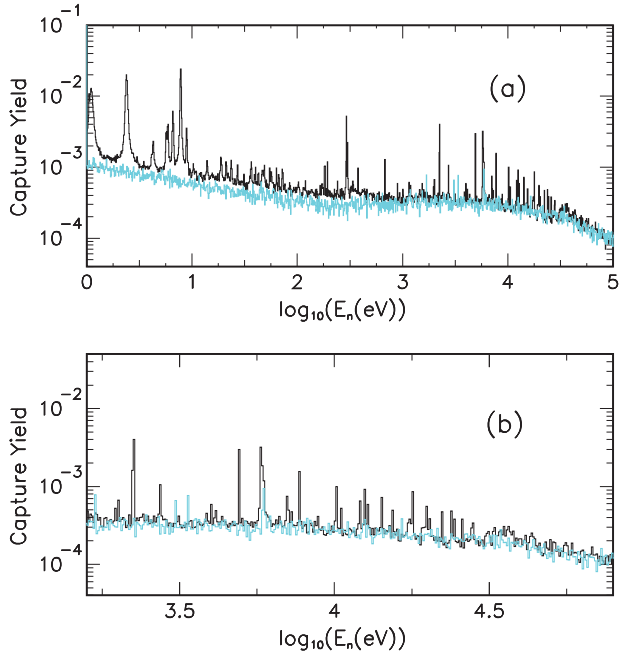

FIG. 1. (Color online) Capture yield (black) and overall background (turquoise) as a function of neutron energy E_n. (a) shows the entire energy range covered by the experiment, and (b) concentrates on the the region of the investigated Zr resonances. All resonances below 2 keV neutron energy are due to Hf and Sn impurities in the sample.

(iii) The dominant background component in the keV region of neutron energies is caused by in-beam γ rays, which are scattered by the sample and detected in the C_6D_6 scintillators. This background was investigated by means of a lead sample, where the capture channel is extremely low and γ scattering is enhanced due to the high atomic number.

(iv) The ambient background was found to be so small that the uncertainty of this contribution could be neglected.

The final capture yield and the overall background are presented in Fig. 1.

III. RESONANCE ANALYSIS AND RESULTS

The experimental yield

$$Y^{\text{expt}} = \frac{Y_w}{N_n E_c} + B$$

is determined by the weighted net count rate Y_w, the effective binding energy E_c, the integrated neutron flux N_n, and the overall background B.

In the resolved resonance region, the experimental yield was analyzed with the $\mathcal{R}$-matrix code SAMMY [29], which was used in the Reich-Moore formalism to extract the individual resonance parameters. Corrections for the energy resolution of the neutron beam, for the Doppler broadening of resonance widths due to the thermal motion, for isotopic and chemical sample impurities, and for self-shielding and neutron multiple scattering are considered in the fits with this code. The Doppler broadening was treated by a free gas model assuming a temperature of 300 K. The effect of potential scattering was calculated using a nuclear radius of 7.2 fm [30]. The resolution function of the n_TOF neutron beam becomes important at energies above 1 keV and leads to low-energy tails in the resonance shapes.

In total 50 resonances could be analyzed in the investigated energy range between 2 and 60 keV. Among these, four resonances were identified for the first time, whereas four of the resonances reported previously [31] have not been observed. Examples illustrating the quality of the fits are summarized in Fig. 2.

The determination of the resonance parameters requires the combination of three measurements: two transmission measurements on samples with different thicknesses (so-called thin and thick [32]) and a capture measurement with a thin sample. In fact, in the asymptotic limit the thin and thick transmission resonance areas and the capture areas are given by

$$A(\text{thin}) \propto g\Gamma_n,$$
$$A(\text{thick}) \propto g\Gamma_n(\Gamma_n + \Gamma_\gamma),$$
$$A_\gamma \propto g\Gamma_n \cdot \Gamma_\gamma/(\Gamma_n + \Gamma_\gamma),$$

where

$$g = \frac{(2J+1)}{(2I_n+1)(2I_{Zr}+1)}$$

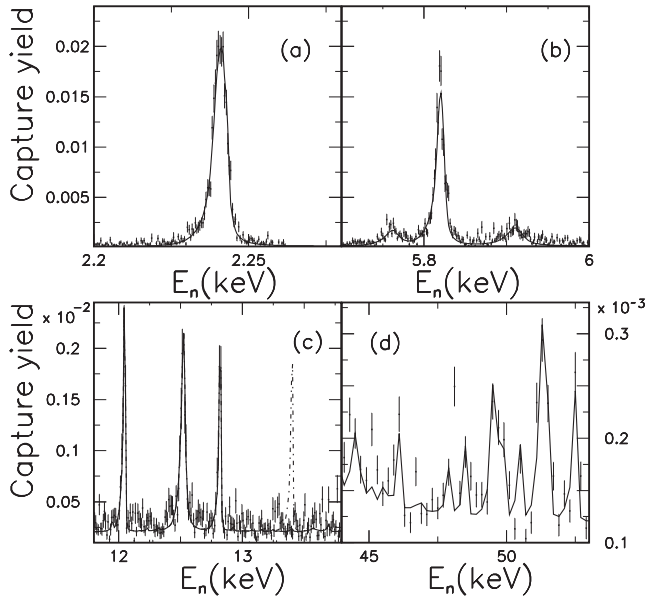

FIG. 2. Examples of fits with the $\mathcal{R}$-matrix code SAMMY (solid lines). (a) and (b) refer to well-established resonances. In (c) the dash-dotted line indicates a previously reported resonance [31], which was not found in the present data. This resonance, which was calculated with the parameters from the JENDL3.3 compilation [35], is probably due to a contamination in the sample of [31]. Finally, (d) shows weak resonances belonging to the upper part of the energy range considered in the present analysis.

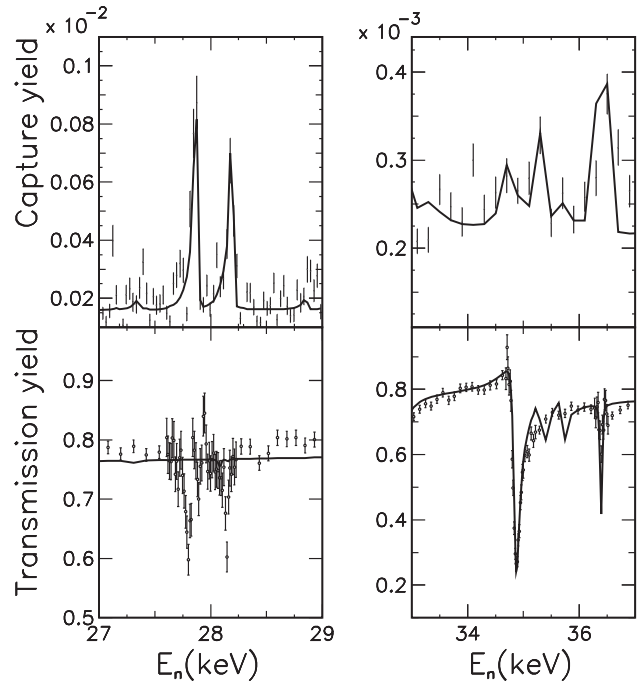

FIG. 3. Upper panels: Capture yield from present measurement [fits made with the $\mathcal{R}$-matrix code SAMMY (solid lines) are superimposed]. Lower panels: Transmission yield from the measurements, of Refs. [31,33] [fits calculated with the parameters from Ref. [31] (solid lines) are superimposed].

is the statistical spin factor determined by the resonance spin J, the spin $I_n = 1/2$ of the incident neutron, and the spin of the target nucleus, $I_{Zr} = 0$; Γ_n and Γ_γ are the neutron and radiative widths, respectively.

Unfortunately a simultaneous analysis with the original transmission data of Ref. [31], in which two samples of ^{94}Zr of different thickness were used, was hampered by the discrepancy between the normalization factors in the data stored in the EXFOR library [33]. However, the transmission data of Ref. [31] were fundamental, not only in order to fix the g and Γ_n values (given that $\Gamma_n \gg \Gamma_\gamma$ in almost all cases), but also in helping the fit of resonances, especially in the region above 30 keV where the statistics of present measurement is poor. Figure 3 shows how transmission data were used for the discrimination of resonances; in particular, data reported in the left panel allowed us to identify two resonances around 28 keV not analyzed in Ref. [31], probably they were not well resolved in the capture data. On the contrary, data reported in the right panel combined with present capture data showed that resonance listed in Ref. [31] at 35.3 and 35.7 keV are probably not physical.

In the resonance analysis here presented, the resonance energies E_R and the radiative widths Γ_γ have been considered as free parameters. In contrast, the neutron widths Γ_n were fixed to the values given in [30], which are based on transmission measurements [31,34]. Similarly, the spin factors were also fixed to the values given in the JENDL-3.3 evaluation [35], because the capture data are not sensitive to the resonance spin.

For a few resonances it was not possible to obtain an acceptable fit of the capture yield if the Γ_n values reported in Ref. [31] were used. For these few cases and for the resonances observed for the first time only the capture kernels are reported instead.

The resonance parameters deduced in the analyses of the background-subtracted capture yield are listed in Table II.

Because of the relatively low cross section of ^{94}Zr, an important part of the final uncertainty is due to limitations in counting statistics. In particular, statistical uncertainties play a relevant role in the analysis of resonances at energies above 30 keV. Nevertheless, a small sample mass was used in the present measurements to avoid systematic uncertainties due to extensive corrections for sample-related effects such as multiple scattering and self-shielding. Because of the decreasing signal/background ratio, the statistical uncertainty grows with neutron energy from ≈4% at 2 keV to ≈8% at 60 keV. Additional sources of uncertainty are due to the energy dependence of the neutron flux and to the fraction of the neutron beam covered by the sample. For the latter contributions an uncertainty of 2% was determined by means of the saturated resonance technique using the 4.9 eV resonance in ^{197}Au. The systematic uncertainty associated with the PHWT, which is essentially due the Monte Carlo simulations for determining the WFs, was determined to be less than 2% as discussed in Ref. [27].

The present results can be compared with previous measurements [31,34,36–38]. References [36,37] limit their analysis to the first resonance at ≈2.2 keV; Ref. [34] lists 11 resonances in the energy range between 2.2 and 14.2 keV and Γ_γ values

TABLE II. Resonance parameters E_R, Γ_n, and Γ_γ and capture kernels K. Uncertainty given on K accounts only for the statistical part. New and unobserved resonances are marked by (*) and (×), respectively.

E_R^a (eV)	J	l	Γ_γ (meV)	$\Delta\Gamma_\gamma$ (%)	Γ_n (eV)	K (meV)	ΔK (%)
2240.54(4)	1/2	0	70.2	1.5	1.27	66.5	1.5
4924.70(7)	1/2	1	175	2.9	0.45	126	3.8
5760.4(6)	1/2	0	54.4	4.4	12.7	54.1	4.4
5817.7(1)	3/2	1	155	2.3	2.66	293	2.2
7071(1)	1/2	0	66.2	5.4	24	66	5.4
7712.3(3)	3/2	1	89.0	4.0	0.8	160	3.8
10135.4(3)	3/2	1	106	3.6	2.3	203	3.4
10562.4(6)	1/2	1	50	7.4	1.7	48.4	7.2
12037.9(5)	1/2	1	127	5.5	3.1	122	5.3
12515.9(7)	3/2	1	118	4.4	10.8	233	4.3
(*) 12809.1(8)						(87.5)	(56)
(×) ≈13390							
14231.7(6)	3/2	1	97	5.7	2.4	187	5.4
15389(1)	1/2	1	142	6.3	8.3	140	6.2
17372(1)	1/2	1	134	7.9	8.35	132	7.8
17903(2)	3/2	1	208	4.8	38.5	415	4.7
19375(16)	1/2	0	104	13	160	104	13
19738(2)						219	55
19855(2)	1/2	0	59	13	6.6	59	13
20236(4)	1/2	1	164	8.5	41	163	8.4
22203(2)	1/2	1	225	7.1	5	215	6.9
22280(4)	1/2	0	62	14	12	62	14
23853(3)	3/2	1	165	6.6	28	327	6.2
24389(3)	1/2	1	200	8.5	28.5	199	8.5
25858(4)						286	4.0
(*) 27836(3)						(239)	(9.2)
(*) 28155(2)						(376)	(9.9)
29755(9)	1/2	0	115	13	61	114	13
30884(5)	1/2	1	184	13	26.5	183	13
31612(7)	3/2	1	92	12	36	184	12
32719(1)	3/2	1	150	13	78	299	13
34749(23)	1/2	0	149	3.8	84	149	3.8
(x) ≈35330							
(x) ≈35700							
36386(3)						306	26
37839(28)	3/2	1	136	30.	46	272	30
38808(1)						229	74
39721(6)						59	60
41563(9)	3/2	1	202	15	69	404	15
43112(1)	3/2	1	308	10	156	614	10
43698(2)						240	15
44408(5)	1/2	0	116	29	5	113	28
(x) ≈45520							
46006(20)						(99)	(27)
47919(2)	3/2	1	65	32	15	129	32
48460(2)	1/2	0	89	24	37	89	24
49463(18)						95	18
(*) 49568(5)						(348)	(55)
51352(4)	1/2	1	94	9.2	25	90	8.9
52405(14)	1/2	1	234	20	35	233	20
54980(19)	1/2	1	103	37	35	102	37
55536(3)	3/2	1	355	14	18	695	13
56608(3)						112	16
58733(20)						660	12

[1]The notation 2240.54(4) used for the resonance energies is equivalent to 2240.54±0.04.

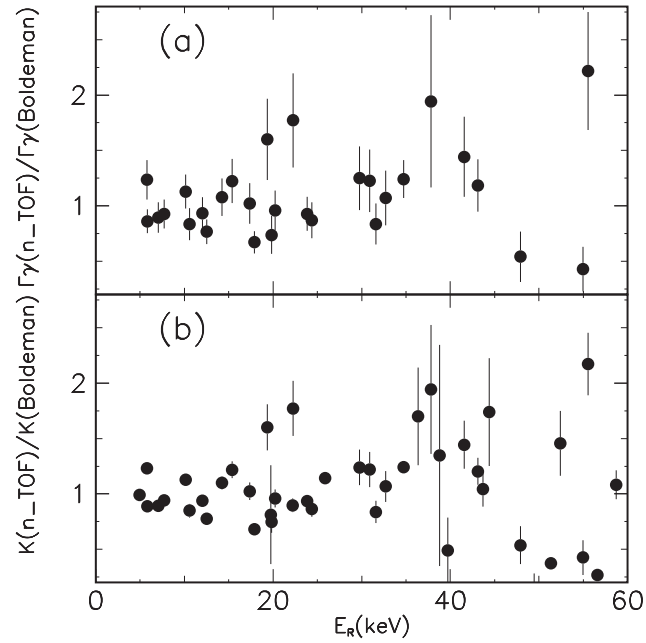

FIG. 4. Ratio between Γ_γ values (top) and capture kernels (bottom) extracted from the present measurement and the results reported by Boldeman *et al.* [31].

were extracted in four cases (resonances at 2.2, 5.8, 7.1, and 12.5 keV). A comprehensive TOF study was performed at the Oak Ridge electron linear accelerator with a pair of fluorocarbon liquid scintillators for the capture and with a ^{6}Li glass scintillator for the transmission measurement [31]. Fluorocarbon (C_6F_6) liquid scintillators were commonly used at that time before C_6D_6 liquid scintillators with a much lower neutron sensitivity became available. In Ref. [31] resonance parameters were extracted in a wide energy range, up to 90 keV. It was found that the neutron widths of all analyzed resonances are much larger than the radiative widths.

Accordingly, the radiative widths Γ_γ listed in Ref. [31] and those extracted in the present measurement can be directly compared. In spite of large differences for some of the resonances, the ratio of the present values and of the results in Ref. [31] is very close to unity on average, as shown in the upper panel of Fig. 4.

The corresponding comparison for the capture kernels shows a very similar trend (bottom panel of Fig. 4). Capture kernels are related to the resonance area and are defined as

$$K = g\frac{\Gamma_n\Gamma_\gamma}{(\Gamma_n + \Gamma_\gamma)}.$$

In first approximation the capture kernels are proportional to Γ_γ because $\Gamma_n \gg \Gamma_\gamma$ in all observed ^{94}Zr resonances. Therefore, the average ratio of the K values is also very close to unity.

IV. MAXWELLIAN-AVERAGED CROSS SECTIONS

For applications in s-process studies the experimental (n, γ) cross sections have to be folded with the neutron velocity

TABLE III. MACS values of ^{94}Zr at $kT = 30$ keV thermal energy. Uncertainties are given for experimental values only.

MACS (mb)	Reference	Year
21±4	[40]	1967
26.6±3.0	[31]	1976
33±5	[38]	1978
25±4	[42]	1983
26.1±1.0	[41]	1990
30.0	[35]	2002
29.1	[43]	2006

distribution in the stellar plasma to obtain the Maxwellian-averaged capture cross sections (MACSs), which are eventually used for calculating the corresponding s abundances. The neutron velocity distribution $\Phi(v)$ is well described by a Maxwell-Boltzmann form [11], because neutrons are quickly thermalized in the dense He-burning stellar plasma, where the s-process takes place.

The folding procedure for obtaining the MACSs requires the capture cross section $\sigma(E_n)$ over a sufficiently wide neutron energy range, ideally from about 100 eV and up to about 500 keV, in order to cover the full temperature ranges of the plausible s-process scenarios sketched in Sec. I, including the highest temperatures reached during shell carbon burning in massive stars [11,39].

The MACS of ^{94}Zr at a thermal energy of $kT = 30$ keV, which have been reported previously on the basis of TOF data [31,38,40], activation results [41,42], and evaluated cross sections [35,43], are summarized in Table III. Most values exhibit sizable uncertainties of 10%–20%, significantly higher than needed for s-process analyses. The only more accurate result, that of Ref. [41], was determined by activation in a quasistellar spectrum for $kT = 25$ keV, which was truncated slightly above 100 keV. This MACS agrees within 4% with the average of all other data.

The MACSs of ^{94}Zr are strongly dependent on the energy and strength of very few prominent resonances. In particular, the two resonances at 5.8 and 17.9 keV contribute 30% and 14% of the total MACSs at thermal energies of 8 and 30 keV, respectively. Although the capture kernels measured in the present work agree with the results of Ref. [31] on average, there are important differences for the crucial cases (Table IV).

MACSs calculated in the present work were extracted by means of routines included in the SAMMY code [29]. Because the neutron energy range covered in this work ends at 60 keV, the present data had to be complemented for calculating the

TABLE IV. Capture kernels K of the most prominent resonances.

	K (meV)	
E_R (keV)	Ref. [31]	This work
5.8	330 ± 30	293 ± 6
17.9	610 ± 60	415 ± 20

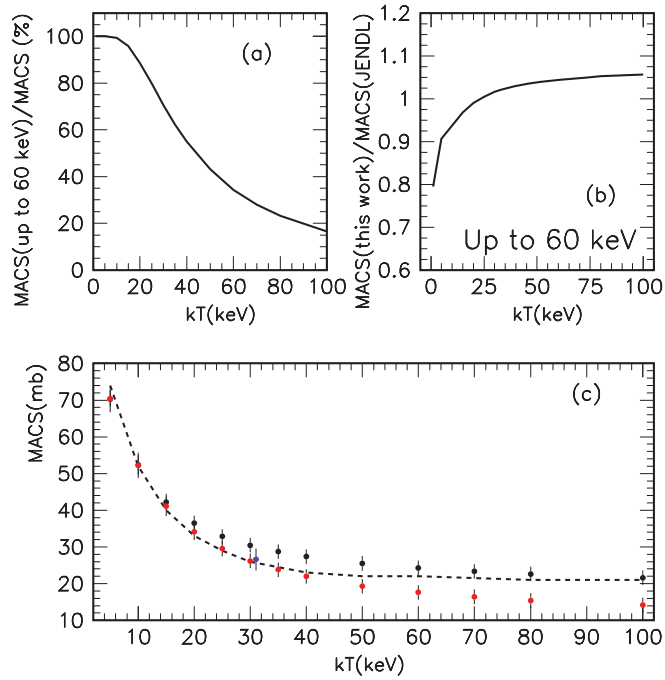

FIG. 5. (Color online) (a) Relative contribution of the present results to the MACSs as a function of thermal energy. (b) Ratio between MACSs based on the present work and those based on evaluated data from the JENDL-3.3 library [35] in the energy range below 60 keV. (c) MACSs for the full energy range using the present results complemented above 60 keV by data of the JENDL-3.3 evaluation (black symbols) or by data of the JENDL-4.0 evaluation (red symbols). The 30 keV value from Ref. [31] (blue symbol) and the MACSs from the compilation of Ref. [11] (dashed line) are shown for comparison (to avoid the overlap of error bars the value from Ref. [31] was displaced along the abscissa from 30 to 31 keV).

MACSs. To illustrate the impact of the new results, first a set of MACS calculations was truncated at 30 (resonance parameters could be determined with uncertainties lower than 10% up to this energy) and 60 keV (Table V). As illustrated in Fig. 5(a), the contribution of the complementary part is negligible at low thermal energies and increases with kT to reach 30% at 30 keV. Compared to an analogously calculated set using the evaluated data from the JENDL-3.3 library [35], Fig. 5(b) shows a pronounced kT dependence, which reflects the differences from the evaluated data [31,35] for the crucial resonances at low kT. At higher thermal energies the weight of these resonances in the MACSs is strongly reduced, due to the increasing contribution of the evaluated cross section for neutron energies above 60 keV. Compared to the values of the compilation of Bao *et al.* [11] and to those obtained from the results of Ref. [35], the present MACSs are smaller at low kT, in particular at 8 keV, the temperature where the ^{13}C(α,n) neutron source is operating in thermally pulsing low-mass AGB stars [3].

For high thermal energies, the use of evaluated cross sections above 60 keV introduces an additional uncertainty, related to differences between various libraries. In particular, while the cross sections in JENDL-3.3 and ENDF/B-VII.0 are similar, the recently released library JENDL-4.0 [44]

TABLE V. MACSs (in mb) calculated for upper integration limits of 30 and 60 keV and for the full energy range compared with MACSs obtained with data from Refs. [11,35].

kT	$E_n \leqslant 30$ keV		$E_n \leqslant 60$ keV		Full range		
(keV)	This work	Ref. [35]	This work	Ref. [35]	This work	Ref. [35]	Ref. [11]
5	69.8 ± 3.5	77.1	70.2 ± 3.5	77.5	70.3 ± 3.5	77.5	74
8	56.2 ± 2.8	61.2	58.5 ± 2.9	63.3	58.5 ± 2.9	63.3	
10	48.2 ± 2.4	52.0	52.0 ± 2.6	55.6	52.3 ± 2.6	55.9	52
15	33.5 ± 1.7	35.5	40.4 ± 2.0	41.7	42.3 ± 2.2	43.5	40
20	24.4 ± 1.2	25.5	32.2 ± 1.6	32.6	36.5 ± 2.0	36.7	33
23	20.5 ± 1.0	21.3	28.4 ± 1.4	28.4	34.0 ± 2.0	34.0	
25	18.4 ± 0.9	19.1	26.2 ± 1.3	26.0	32.9 ± 2.0	32.6	29
30	14.3 ± 0.7	14.7	21.6 ± 1.1	21.2	30.5 ± 2.0	30.0	26
40	9.3 ± 0.5	9.5	15.2 ± 0.8	14.8	27.4 ± 2.0	26.8	23
50	5.5 ± 0.3	6.5	11.1 ± 0.6	10.8	25.5 ± 2.0	25.0	22
60	4.5 ± 0.2	4.8	8.6 ± 0.4	8.2	24.3 ± 2.0	23.8	22
80	2.8 ± 0.1	2.8	5.4 ± 0.3	5.2	22.6 ± 2.0	22.3	21
100	1.9 ± 0.1	1.9	3.7 ± 0.2	3.5	21.6 ± 2.0	21.4	21

contains substantially smaller evaluated cross sections. The effect can be clearly seen in Fig. 5(c), which shows the MACSs calculated with the n_TOF data complemented with evaluated cross sections from JENDL-3.3 (black symbols) and from JENDL-4.0 (red symbol). For comparison, the compilation from Bao *et al.* [11] is also shown in the figure, together with the MACS of Ref. [31] (blue symbol). While, as expected, the choice of the evaluated file has little influence on low-temperature MACSs, an increasing difference is observed at higher thermal energy, reflecting the differences in the evaluated cross sections. In particular, the MACSs calculated with JENDL-4.0 extrapolation are systematically lower than the one obtained using JENDL-3.3, with the difference increasing for increasing thermal energy. Compared with the compilations of Bao *et al.*, the n_TOF results show a good agreement below 50 keV thermal energy when extrapolated with JENDL-4.0, while a much better agreement is observed at higher temperatures when complemented with JENDL-3.3. It is clear that the differences in the evaluated cross sections make it difficult at the moment to obtain a clear indication of the value of the MACSs at high thermal energy. New data at high energy would be very useful in this respect, since they would allow a reduction of the uncertainty on the calculated MACSs, by discriminating between different evaluations.

V. ASTROPHYSICAL IMPLICATIONS

The changes in the MACS values imply that about 10% more ^{94}Zr is produced in the interpulse period between He shell flashes in thermally pulsing low-mass AGB stars by the ^{13}C(α, n) neutron source due to the lower MACS at $kT =$ 8 keV. The final abundance is established, however, during each subsequent He shell flash, when the ^{22}Ne(α, n) source is activated at about 23 keV, where the MACS is about 10% higher compared to the data of Ref. [11].

Accordingly, one finds a slightly lower s-process production of ^{94}Zr if the calculation of Ref. [4] is repeated with the present MACSs. The increase of the s abundance at $kT = 8$ keV is compensated at $kT = 23$ keV in spite of the lower neutron fluence provided by the ^{22}Ne(α, n) source. In the end, the 8% overabundance obtained by Arlandini *et al.* [4] was found to decrease by 2%.

The reason for this problem resides in the approach of Arlandini *et al.* to reproduce the s component of the solar abundance distribution with a particular stellar model. If the solar s component is, instead, determined within a realistic treatment of Galactic evolution, including the s-process yields from AGB stars of different mass and metallicity and accounting for their respective lifetimes [45,46], it turned out that the s-process components of Sr-Y-Zr are about 20%–30% lower than the values reported in Ref. [4]. Within this difference, the higher s component of ^{94}Zr implied by the present MACSs is well consistent with its observed solar abundance.

VI. CONCLUSIONS

The (n, γ) cross section of ^{94}Zr has been measured with improved accuracy between 1 eV and 60 keV neutron energy at the n_TOF facility at CERN. The parameters of 50 resonances (four newly identified) were determined in the neutron energy range between 2 and 60 keV.

At thermal energies of 8 and 23 keV, typical for the s process in thermally pulsing low-mass AGB stars, the MACS values were found to be slightly lower and 10% higher than reported in current compilations [11,39], respectively. These differences are relaxing the overabundance problem for ^{94}Zr reported by Arlandini *et al.* [4], but are well compatible with the expectation from a chemical evolution model of the Galaxy [45,46].

ACKNOWLEDGMENTS

This work was supported by the EC under Contract No. FIKW-CT-2000-00107 and by the funding agencies of the participating institutes.

[1] E. M. Burbidge, G. R. Burbidge, W. A. Fowler, and F. Hoyle, Rev. Mod. Phys. **29**, 547 (1957).
[2] C. M. Raiteri, R. Gallino, M. Busso, D. Neuberger, and F. Käppeler, Astrophys. J. **419**, 207 (1993).
[3] R. Gallino, C. Arlandini, M. Busso, M. Lugaro, C. Travaglio, O. Straniero, A. Chieffi, and M. Limongi, Astrophys. J. **497**, 388 (1998).
[4] C. Arlandini, F. Käppeler, K. Wisshak, R. Gallino, M. Lugaro, M. Busso, and O. Straniero, Astrophys. J. **525**, 886 (1999).
[5] M. Lugaro, F. Herwig, J. C. Lattanzio, R. Gallino, and O. Straniero, Astrophys. J. **586**, 1305 (2003).
[6] A. G. W. Cameron, Space Sci. Rev. **15**, 121 (1973).
[7] F. Käppeler, Prog. Nucl. Part. Phys. **43**, 419 (1999).
[8] D. Lambert *et al*., Astrophys. J. **450**, 302 (1995).
[9] E. Zinner, Annu. Rev. Earth Planet. Sci. **26**, 147 (1998).
[10] M. Lugaro, A. M. Davis, R. Gallino, J. Pellin, O. Straniero, and F. Käppeler, Astrophys. J. **593**, 486 (2003).
[11] Z. Y. Bao, H. Beer, F. Käppeler, F. Voss, K. Wisshak, and T. Rauscher, At. Data Nucl. Data Tables **76**, 70 (2000).
[12] G. Tagliente *et al*., Phys. Rev. C **77**, 035802 (2008).
[13] G. Tagliente *et al*., Phys. Rev. C **78**, 045804 (2008).
[14] G. Tagliente *et al*., Phys. Rev. C **81**, 055801 (2010).
[15] A. M. Davis, G. K. Nicolussi, M. J. Pellin, R. S. Lewis, and R. N. Clayton, in *Nuclei in the Cosmos V*, edited by N. Prantzos and H. Harissopulos (Editions Frontieres, Paris, 1998), p. 563.
[16] R. J. Stancliffe, M. Lugaro, A. I. Karakas, and C. A. Tout, Nucl. Phys. A **758**, 569 (2005).
[17] C. Borcea *et al*., Nucl. Instrum. Methods Phys. Res., Sect. A **513**, 523 (2003).
[18] U. Abbondanno *et al*., CERN n_TOF facility: Performance Report No. CERN-SL-2002-053 ECT, 2003.
[19] J. Pancin *et al*., Nucl. Instrum. Methods Phys. Res., Sect. A **524**, 102 (2004).
[20] The n_TOF Collaboration, Report No. CERN INTC-O-011, CERN, 2003.
[21] G. Lorusso *et al*., Nucl. Instrum. Methods Phys. Res., Sect. A **532**, 622 (2004).
[22] S. Marrone *et al*., Nucl. Instrum. Methods Phys. Res., Sect. A **517**, 389 (2004).
[23] R. Plag, M. Heil, F. Käppeler, P. Pavlopoulos, R. Reifarth, and K. Wisshak, Nucl. Instrum. Methods Phys. Res., Sect. A **496**, 425 (2003).
[24] U. Abbondanno *et al*., Nucl. Instrum. Methods Phys. Res., Sect. A **538**, 692 (2005).
[25] F. Corvi *et al*., Nucl. Sci. Eng. **107**, 272 (1991).
[26] J. N. Wilson *et al*., Nucl. Instrum. Methods Phys. Res., Sect. A **511**, 388 (2003).
[27] U. Abbondanno *et al*., Nucl. Instrum. Methods Phys. Res., Sect. A **521**, 454 (2004).
[28] R. L. Macklin and J. Halperin, Phys. Rev. C **14**, 1389 (1976).
[29] N. M. Larson, "Updated Users' Guide for SAMMY: Multilevel *R*-matrix Fits to Neutron Data Using Bayes' Equations," computer code SAMMY, Report No. ORNL/TM-9179/R7, Oak Ridge National Laboratory, 2006.
[30] S. F. Mughabghab, *Atlas of Neutron Resonances, Resonance Parameters and Thermal Cross Sections* $Z = 1$*–100* (Elsevier Science, Amsterdam, 2006).
[31] J. W. Boldeman, A. R. de L. Musgrove, B. J. Allen, J. A. Harvey, and R. L. Macklin, Nucl. Phys. A **269**, 31 (1976).
[32] J. E. Lynn, *Theory of Neutron Resonance Reactions* (Clarendon Press, Oxford, 1968); E. R. Rae *et al*. Nucl. Phys. **5**, 89 (1958).
[33] [http://www-nds.iaea.org/exfor/exfor.htm].
[34] Z. M. Bartolome *et al*., Nucl. Sci. Eng. **37**, 137 (1969).
[35] K. Shibata *et al*., J. Nucl. Sci. Technol. **39**, 1125 (2002).
[36] S. P. Kapchigashev, Sov. At. Energy **19**, 1212 (1965).
[37] G. Leinweber *et al*., Nucl. Sci. Eng. **134**, 50 (2000).
[38] A. de L. Musgrove, B. Allen, J. Boldeman, and R. L. Macklin, in *Neutron Physics and Nuclear Data for Reactors and Other Applied Purposes* (OECD, Paris, 1978), p. 449.
[39] [http://www.kadonis.org].
[40] R. L. Macklin and J. H. Gibbons, Phys. Rev. **159**, 1007 (1967).
[41] K. Toukan and F. Käppeler, Astrophys. J. **348**, 357 (1990).
[42] J. Wyrick and W. Poenitz, Technical Report No. ANL-83-4, Argonne National Laboratory, 1983, p. 196.
[43] M. B. Chadwick, P. Oblozinsky, and M. Herman, Nucl. Data Sheets **107**, 2931 (2006).
[44] K. Shibata *et al*., J. Nucl. Sci. Technol. **48**, 1 (2011).
[45] C. Travaglio, R. Gallino, E. Arnone, J. J. Cowan, J. Jordan, and C. Sneden, Astrophys. J. **601**, 864 (2004).
[46] A. Serminato, R. Gallino, C. Travaglio, S. Bisterzo, and O. Straniero, Publ. Astron. Soc. Australia **26**, 153 (2009).